Role of configurational entropy on CoNi based superalloys for sustainable applications

Ahad Mohammadzadeh[a, b*], Akbar Heidarzadeh[c], Hailey Becker[d], Jorge Valilla Robles[a], Alberto Meza[a], Manuel Avella[a], Miguel A. Monclús[a], Damien Tourret[a], José Manuel Torralba[a, e]

[a] *Imdea Materials Institute, Calle Eric Kandel, 2, 28906, Getafe, Madrid, Spain*

[b] *Department of Materials Engineering, Faculty of Engineering, University of Maragheh, Maragheh, P.O. Box 83111-55181, Iran*

[c] *Department of Materials Engineering, Azarbaijan Shahid Madani University, Tabriz 53714-161, Iran*

[d] *Department of Chemical Engineering and Materials Science, Michigan State University, USA*

[e] *Universidad Carlos III de Madrid, Av. Universidad 30, 28911 Leganés*

**Corresponding Author. E-mail address: ahad.mohammadzadeh@imdea.org*

Abstract

A comprehensive literature review on recently rediscovered Co and/or CoNi-based superalloys strengthed by γ′ phase (with an $L1_2$ crystallographic structure) revealed that there is a relationship between the configurational entropy of the system and γ′ solvus temperature. This study was conducted on a high Cr CoNi based superalloy system with high configurational entropy to implement our hypothesis based on the sustainable metallurgy framework. After thermodynamical modeling to design the chemical compositions, vacuum casting, homogenization, solutionizing, and aging heat treatments were performed to produce desired alloys. Microstructures were evaluated using a scanning electron microscope (SEM), electron backscattered diffraction (EBSD), scanning transmission electron microscope (STEM), and differential thermal analysis (DTA). Microhardness and nanoindentation tests were employed to measure the mechanical properties. The results showed that both the configurational entropy and type of alloying elements determine the final high temperature performance of the alloys. It was revealed that to enhance the higher γ′ solvus temperature, the configurational entropy should be increased by adding γ′ stabilizing

elements. The microstructural and mechanical characteristics of designed alloys before and after heat treatments are discussed in detail. The outcome of this study is beneficial to develop cobalt-based high entropy superalloys with appropriate processing windows and freezing range for ***advanced sustainable manufacturing*** purposes such as selective laser melting.

Keywords: CoNi-based superalloys; Configurational entropy; CALPHAD method; Microstructure.

1 Introduction

Improving energy efficiency along with capturing and storing greenhouse gas emissions such as CO_2 is the essential duty of all industrial sectors. It requires new technologies, whose ultimate aim is the zero-emission power plant, which depends strongly on the availability of suitable materials such as superalloys and their development by new processing routes [1, 2]. Superalloys have attracted immense attention in the aerospace and power generation industries due to outstanding combinations of mechanical and chemical properties [2]. They are successful today because they have solved pressing demands for durability and strength in machines and systems that were barely imaginable a hundred years ago [3]. Among the superalloys, Ni-based superalloys, the earliest and best-developed superalloy family with a two-phase microstructure consisting of a gamma (γ) matrix and a strengthening phase called gamma prime (γ') (with $L1_2$ crystallography), gained lots of attention due to high temperature capability. For example, 40-50 wt. % of modern aircrafts are made of Ni-based superalloys [3]. However, advances in mature Ni superalloys are restricted by approaching the γ' solvus temperature to the Ni melting point, which is a limitation to ***improving their sustainability*** (energy efficiencies and reducing CO_2 emissions). Fortunately, the introduced novel $L1_2$-strengthened Co-based superalloys, which are in the initial stage of development, are

believed to be an excellent replacement for the Ni-based superalloys because of their higher melting points (50-150 °C higher than Ni superalloys) [4, 5].

Since the rediscovery of the γ'-Co_3(Al, W) phase in 2006 [6], significant efforts have been made to understand the thermodynamic, physical, mechanical, and environmental properties of the γ' strengthened Co-based superalloys [3, 7]. In addition, some researchers have developed novel Co-based superalloys to increase the γ′ solvus temperature [5, 8]. According to the historical development of superalloys [9] and after a comprehensive analysis of data published in the literatures [6, 8, 10-19], it is very intersting that there is a relationship between the configurational entropy (ΔS^{mix}) and γ′ solvus temperature in Co based superalloys, as shown in Fig. 1. For example, in a Co-based superalloy, by enhancing ΔS^{mix} from 0.613R (four elements) to 1.298R (six elements), γ′ solvus temperature rises from 870 °C to 1128 °C [10]. From Fig. 1, one can conclude that the design of novel alloys based on the high entropy concept [19], i.e. production of high entropy alloys (HEAs) may overcome the drawbacks of γ′ solvus temperature in the application of Co-based superalloys. Thus, the development of Co based superalloys/HEAs on the successful platform established for Ni based superalloys can be an acceleration towards the ***advanced sustainable materials.*** The other point that can be extracted from Fig. 1 is the fact that even at the same amount of entropy, some alloys in each category can withstand higher temperatures than others, which suggests that selecting the appropriate elements and their concentrations is critical. Therefore, it is essential to have a fundamental understanding of the effect of different elements to develop appropriate Co based high entropy superalloys (HESA) with outstanding properties, which requires more studies in the field.

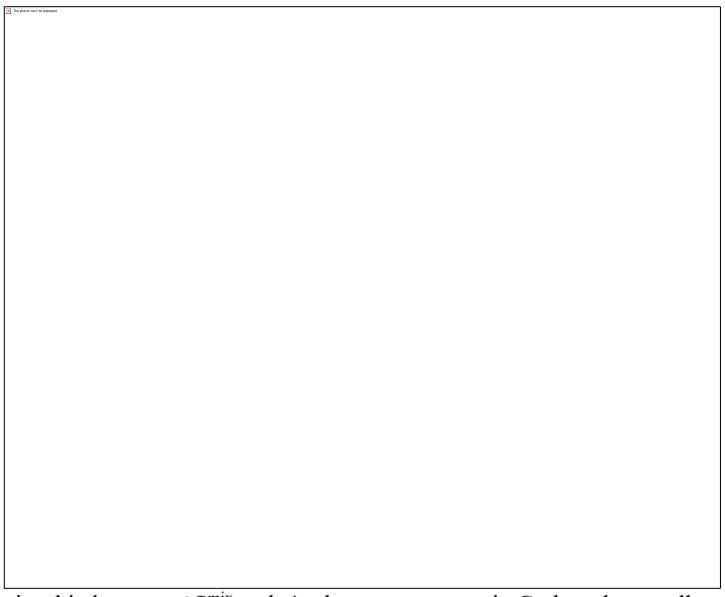

Fig. 1. Relationship between ΔS^{mix} and γ′ solvus temperature in Co-based superalloys, data from literature [6, 8, 10-21].

A six-component Co-Ni-Al-Ti-Ta-W alloying system has been recognized as a promising CoNi based superalloy with higher γ′ solvus temperature without forming any secondary phases at high temperatures [7, 8]. In addition, decreasing the density (critical for aerospace applications) and increasing the oxidation resistance should be considered during alloy design. The density reduction can be reached by replacing W with other alloying elements such as Mo, Nb, V, and Ti [22-26]. In the case of oxidation resistance, it has been reported that adding Cr besides Al to the multicomponent Co-based superalloys is necessary, which has caused the development of high Cr-cobalt-based superalloys [18, 27]. For example, Zhuang et al. [18] designed an alloy with high temperature oxidation and corrosion resistance based on the calculation of phase diagrams (CALPHAD) method with the composition of Co-30Ni-8Al-4Ti-2W-1Ta-14Cr (all chemical composition quantities are in at. %). They followed the same strategy compared to commercially

available wrought Ni based superalloys, which require setting Al and Al+Cr content equal to or higher than 4.5 at. % and 21 at. %, respectively. Liu et al. [15] optimized an alloy using a machine learning method, obtaining an optimum content of 2 at. % Cr and 12 at. % Al with a γ′ solvus temperature of 1266.5 °C and γ′ volume fraction of 74.5 % after aging at 1000 °C for 1000 h. They reported that the desired oxidation resistance of the developed CoNi-based superalloy is related to the formation of a protective alumina layer at 1000 °C. Additionally, Bauer et al. [28] have developed an alloy with a nominal composition of Co-9Al-8W-2Ta-2Cr, and they have found that Cr reduced the γ′ solvus temperature slightly since it tends to distribute in face-centered cubic (FCC) γ phase. Thus, this negative effect of Cr should be solved by adding other elements to Co-based multicomponent alloys. Li et al. [24] have reported that Cr can moderate the negative effect of W on γ′ volume fraction in CoNi superalloy by changing the partitioning characteristics of Al and Ti. Recently, Cao et al. [20] have introduced a novel multicomponent W-free Co-rich HEA containing 10 at. % Cr. They have reported that the γ′ solvus temperature can be increased up to 1125 °C, which was higher than those reported in the literature compared with the W-free Co-based superalloys.

Due to the importance of γ′ solvus temperature in high Cr CoNi-based superalloys, this study evaluates the effect of ΔS^{mix} on the γ′ solvus temperature compared to those reported in the literature [3, 20, 24, 28]. Thermodynamical modeling (CALPHAD method) has been employed to design new CoNi-based high entropy superalloys (CoNiHESAs) based on the criteria of ΔS^{mix} values higher than 1.5R and considering alloying elements with high temperature capability and low density. The outcome of this research will introduce a new design strategy based on the high ΔS^{mix} and CALPHAD method.

2 Materials and methods

2.1 CALPHAD calculations

Thermoclac software (version 2022?) with the TCNI8 database (2018?) was utilized for thermodynamical calculation and to evaluate its ability to develop CoNi-based HESAs. The criteria in the design steps have been considered as follows: a ΔS^{mix} value of higher than 1.5R, higher gamma prime solvus temperature, lower density, and avoiding the formation of topologically close-packed phases (TCPs). To implement our suggested hypothesis, we started our calculation with 41Co-30Ni-8Al-4Ti-2W-1Ta-14Cr septenary alloy [18] with a ΔS^{mix} of 1.457R. To increase the amount of ΔS^{mix}, the Ni content was increased to 35 at. % at the expense of Co, the Ta concentration was increased to 2 at. % at the expense of Cr, and introducing the V at the expense of Cr. In this regard, one septenary and two octonaries of multicomponent CoNi based HESAs namely CNS1, CNS2, and CNS3 were designed.

Commented [1]:

2.2 Experimental procedure

To validate the thermodynamical calculations, the designed alloys were produced via vacuum arc remelting (VAR) under a high-purity Ar atmosphere, those chemical compositions are given in Table 1. To compensate for the Al evaporation during melting, the mass of Al was considered 5% higher than its nominal values. The alloys were inverted and melted/remelted four times to attain homogeneous chemical compositions. After casting, alloys were homogenized at 1250 °C for 24 hours followed by air and furnace cooling. Aging was performed on the air-cooled samples at 900 °C for 24 hours followed by quenching in water.

A FEI Helios Nanolab 600i scanning electron microscope (SEM) equipped with energy-dispersive X-ray spectroscopy (EDS) and Nordlys EBSD detectors was utilized to characterize the microstructural characteristics of the as-cast, homogenized, and aged samples. The samples were

mechanically ground and polished using a series of diamond pastes down to 1 μm grit and then a final polishing by an oxide particle suspension (OPS, 0.04 μm) to improve the sample surface for EBSD analysis. For detecting the γ and γ′ phases in homogenized and aged conditions, samples were etched with a Kalling's solution. ImageJ software was employed to determine the volume fraction of the γ′ phase in SEM images. AZtecHKL acquisition software was utilized to analyze the EBSD data. For further microstructural details, i.e. the morphology and elemental partitioning in γ and γ′ phases, an FEI Talos F200X 200keV field emission scanning/transmission electron microscope (STEM) was employed. The STEM samples were thinned with grinding paper to approximately 50 μm and subsequently punched into 3 mm disks. The final thinning was performed using a Struers TenuPol-5 electropolishing unit with a solution of 40 mL acetic acid, 80 mL perchloric acid, and 880 mL of ethanol at -25 °C and 22.5 V. Differential thermal analysis (DTA, model: Setsys Evolution TGA & DTA/DSC Setaram) was carried out on the aged samples to measure the solidus, liquidus, and γ′ solvus temperatures. The DTA experiments have performed in an alumina crucible with a heating rate of 10 °C/min under an Ar atmosphere protection.

The mechanical properties of the as-cast, homogenized, and aged samples were evaluated by Vickers hardness and nanoindentation tests. Vickers hardness was measured using an INNOVATEST instrument by applying 1 kg load and a dwell time of 15 s at room temperature. Five hardness measurements were carried out per sample, and the average values were considered. In the case of the as-cast and homogenized samples, nanoindentation arrays were made using a Hysitron TI 950 Triboindenter equipped with a diamond Berkovich indenter. 22 × 22 arrays were performed with a 3.5 μm spacing using a 0.1 s linear ramp to a peak force of 2 mN, a 0.1 s hold time, and a 0.1 s linear unloading ramp, leading to depths from ? nm.

For the aged samples, nanoindentation tests were also performed in load-controlled mode using a load function consisting of 10 s load, 5 s hold, and 2 s unload, using a maximum load of 500 mN. The reported nanoindentation hardness (H_{ind}) and reduced modulus values are the average of at least 9 indents and were obtained using the produced force-displacement curves using the Oliver and Pharr method [29].

3 Results

3.1 CALPHAD calculations

The initial calculated isopleth sections of the designed alloys are depicted in Fig. 2. These sections were calculated for XCo-YNi-8Al-4Ti-2Ta-2W-13Cr (CNS1), XCo-YNi-8Al-4Ti-4V-2Ta-2W-9Cr (CNS2), and XCo-YNi-8Al-4Ti-4V-2Ta-2W-12Cr (CNS3) compositions. The isopleth sections were calculated by varying the Ni content at the expense of Co and they were plotted as a function of the Ni content varying from 30 at. % to 40 at. % at a temperature range from 600 °C to 1500 °C. According to Fig. 2, by increasing the Ni content, the γ′ solvus temperature was increased. Also, some secondary phases, e.g. B_2, $D0_{19}$, $D0_{24}$, Laves, and σ were existed in the selected temperature and composition ranges. The $D0_{19}$, $D0_{24}$, and Laves phases were excluded from calculations to optimize the CALPHAD results since they have not been reported in this series of CoNi-based superalloys [18, 27, 30].

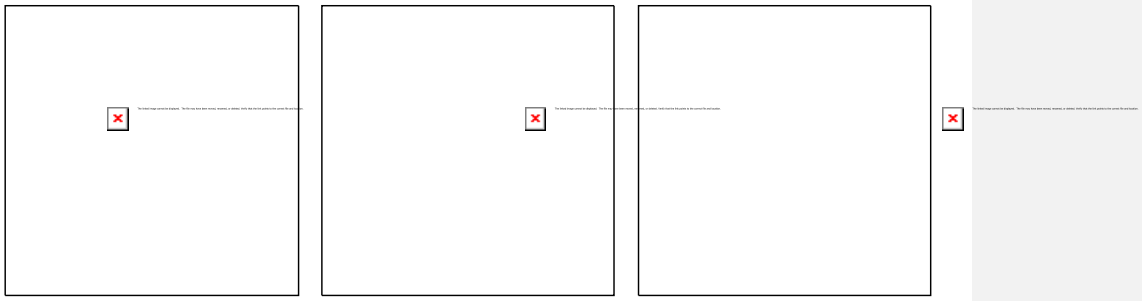

Fig. 2. Initially calculated isopleth sections showing the effect of Ni variation at the expense of Co from 600 °C to 1500 °C.

The optimized isopleth sections of the designed alloys and the corresponding mass fractions of the γ, γ′, B_2, σ, μ, and liquid phases are represented in Fig. 3. From the optimized isopleth sections, there were wide areas of γ and γ+ γ′ suggesting appropriate regions for performing solutionizing and aging heat treatments. To increase the ΔS^{mix}, a balance between Co and Ni is required, particularly in a septenary system. So, the amount of Ni for the CNS1 alloy was adjusted to 35 at. % (Fig. 3a). It is worth noting that at a Ni content of 35 at. % it is possible to avoid the formation of B_2, σ, and μ phases at temperatures higher than 900 °C (Fig. 3d). The CNS2 alloy was developed with the aim of increasing the number of elements to eight by V addition at the expense of the Cr. Consequently, by adding of V, the amount of the ΔS^{mix} was enhanced to 1.568R (Table 1). Notably, the effect of V as a lightweight γ′ stabilizer [28] on microstructural features of this series of CoNi-based superalloys has not yet been investigated.

In the case of octonaries systems and formation possibility of the secondary phases (B_2 and μ phases), the amount of Ni was set at 35 at.% for CNS2 alloy (Fig. 3b). From Fig. 3b, the B_2 phase bubble shifted to the left as a result of the decreasing Cr and the addition of the V. Furthermore,

according to the mass fraction plot of the CNS2 alloy (Fig. 3e), it is possible to avoid μ phase formation at temperatures higher than 800 °C. CNS3 alloy with a ΔS^{mix} of 1.568R, and higher amount of Co (40 at. %), and Ni content of 30 at. % was designed in order to evaluate the effect of Ni on the microstructural features and phase transformations compared to the CNS2 alloy at a same level of the ΔS^{mix}. From (Fig. 3c), the formation possibility of the B_2, σ, and μ phases was high. Referring to mass fraction calculations for CNS3 alloy (Fig. 3f) there was a narrow window for the formation of the B_2 phase (990 °C to 1120 °C) and it could be possible to avoid this phase after homogenization treatment. σ and μ phases could be avoided at temperatures higher than 880 °C.

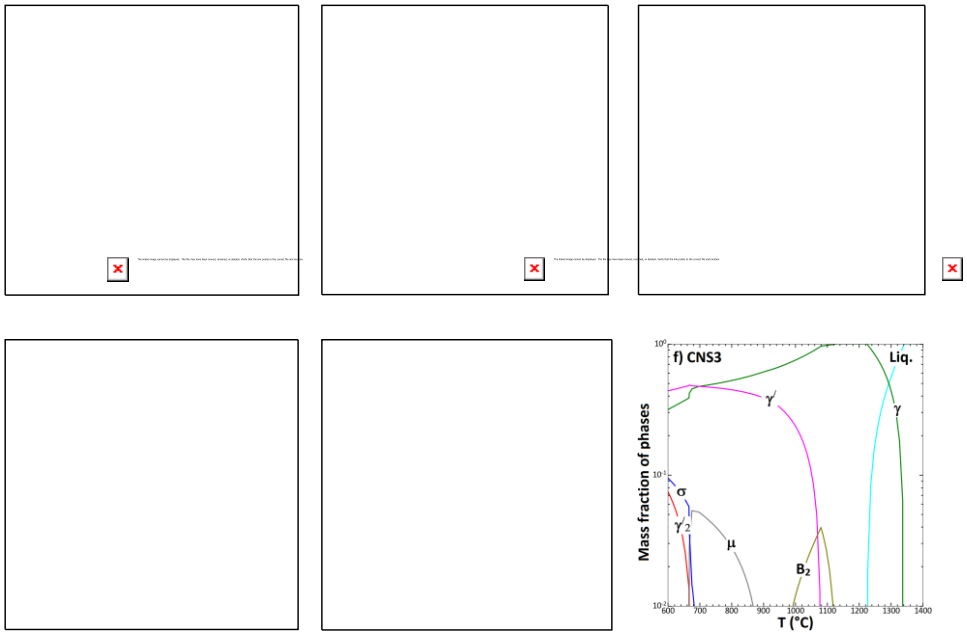

Fig. 3. Optimized isopleth sections (a, c, and e) showing the effect of Ni variation at the expense of Co and corresponding mass fractions as a function of temperature for CNS1, CNS2, and CNS3, respectively.

3.1 Validation of the CALPHAD calculations

A typical SEM back-scattered image of the as-cast CNS1 alloy is shown in Fig. 4a unravelling a dendritic structure with evidence of microsegregation between dendritic and interdendritic spaces e.g. indicated by white arrows. EBSD and EDS analyses were carried out on the as-cast alloys to identify the phases present in the microstructure. The EBSD phase map (Fig. 4b) confirmed the existence of a secondary phase with a body centered cubic (BCC) crystallographic structure. Considering the EDS mapping analysis (Fig. 4c), the BCC phase was an Al-rich intermetallic within the segregation regions. Referring to the isopleth section of CNS1 (Fig. 3a), the possible phase that could be formed during solidification is the B_2 phase, which is in agreement with the EBSD and EDS results.

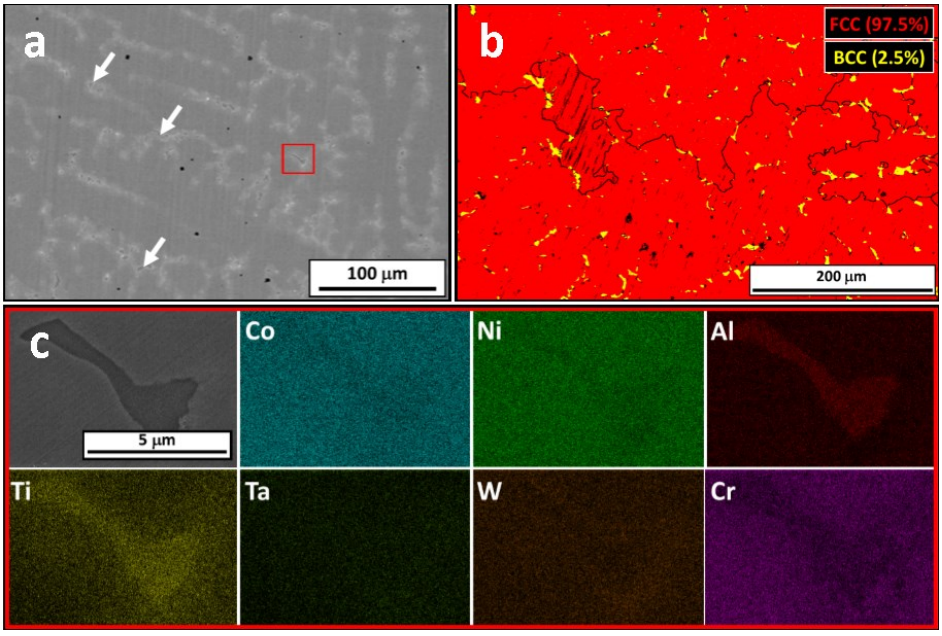

Fig. 4. Microstructural characterization of the as-cast CNS1 alloy, (a) SEM back-scattered image, (b) EBSD phase map, and (c) EDS mapping analysis of the area indicated by the red rectangle in (a). In (b)

the high angle grain boundaries (θ≥15°) are drawn by black lines. The step size of the EBSD scan was 0.4 μm.

To homogenize the chemical composition, dissolve the B_2 phase, and obtain a uniform microstructure, the as-cast alloys were solutionized at 1250 °C for 24 h following air or furnace cooling. The SEM micrographs of the solutionized samples are shown in Fig. 5, which indicated a more refined γ/γ′ distribution in the air-cooled condition (Figs. 5a-c) compared to that of the furnace-cooled condition (Figs. 5d-f). The coarser γ′ after solutionizing heat treatment is not suitable for performing aging heat treatment, and hence the air-cooled samples were selected for further study. From EBSD phase maps of the air-cooled samples, depicted in Fig. 6, the solutionizing was successful because the matrix's main phase had an FCC structure (corresponding to the γ and γ′ phases), and there was a minor amount of B_2 phase (≤0.2%) with BCC structure. The chemical compositions of the solutionized samples (Table 1) indicated that the nominal values were very close to the experimentally measured values. In addition, the calculated ΔS^{mix} based on both the nominal and experimental values is summarized in Table 1, which revealed the higher ΔS^{mix} values for CNS2 and CNS3 alloys compared to that of the CNS1 alloy.

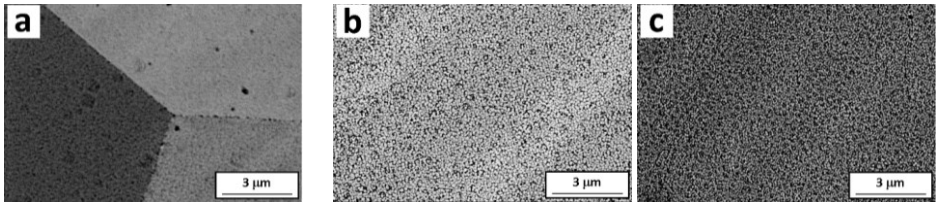

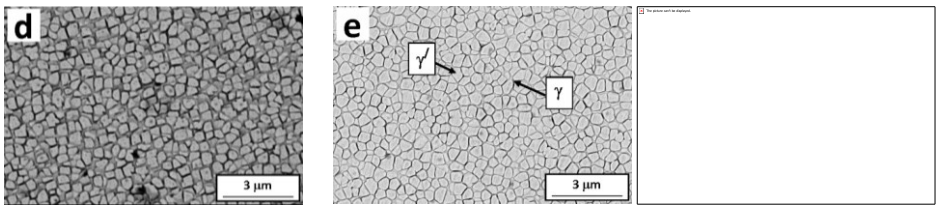

Fig. 5. FE-SEM micrographs of the solutionized samples at 1250 °C for 24 h followed by air-cooling (a, b, and c) and furnace-cooling (d, e, and f), respectively for CNS1, CNS2, and CNS3.

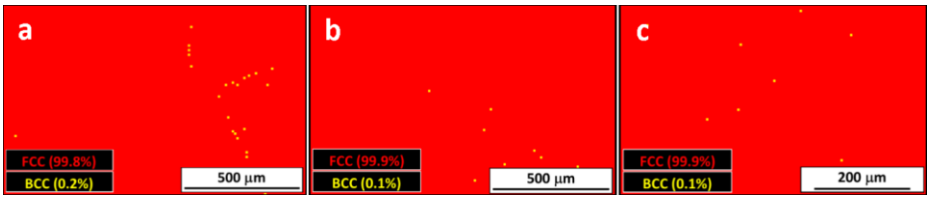

Fig. 6. EBSD phase maps of the homogenized samples at 1250 °C for 24 h followed by air cooling, a) CNS1, b) CNS2, and c) CNS3.

Table 1. The nominal and experimental (measured by EDS point analysis) chemical composition of the homogenized/air-cooled samples in conjunction with their ΔS^{mix}. No. and Ex. refer to the nominal and experimental values.

Sample codes		Chemical composition (at. %)								$\Delta S^{mix.}$
		Co	Ni	Al	Ti	V	W	Ta	Cr	
CNS1	No.	36	35	8	4	0	2	2	13	1.488R
	Ex.	36.10±0.15	34.45±0.32	7.92±0.09	4.35±0.08	0	1.71±0.1	2.21±0.1	13.26±0.21	1.494R
CNS2	No.	36	35	8	4	4	2	2	9	1.568R
	Ex.	35.97±0.4	34.49±0.42	7.68±0.3	4.36±0.23	4.27±0.06	1.87±0.12	2.06±0.08	9.31±0.05	1.579R
CNS3	No.	40	30	8	4	2	2	2	12	1.568R
	Ex.	40.15±0.27	29.33±0.26	7.81±0.26	4.1±0.01	2.12±0.02	2.06±0.11	2.05±0.10	12.4±0.04	1.556R

3.2 Aging

The DTA curves of aged samples (Fig. 7) were employed to measure the actual values of the solidus, liquidus, and gamma prime solvus temperatures, i.e. T_S, T_L, and $T_{\gamma'}$, respectively. The

actual and predicted values of T_S, T_L, and $T_{\gamma'}$ in conjunction with the corresponding freezing range and hot processing window for aged samples are summarized in Table 2. From Fig. 7 and Table 2, CNS2 sample showed higher $T_{\gamma'}$ (1165 °C) compared to those of CNS1 (1150 °C) and CNS3 (1134 °C) samples. Moreover, the hot processing window between 120 °C-141 °C and freezing range between 61 °C-71 °C (Table 2) indicated the ***high capability of the developed alloys for sustainable manufacturing purposes***, e.g. powder bed fiusion techniques.

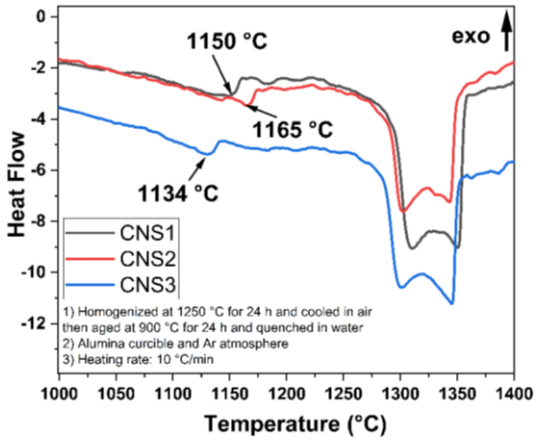

Fig. 7. Differential thermal analysis (DTA) curves of different aged samples.

Table 2. Predicted and actual values of the solidus, liquidus, and gamma prime solvus temperatures of the aged samples (T_S, T_L, and $T_{\gamma'}$, respectively) in conjunction with corresponding freezing range and hot processing window.

Sample code	Calculation method	T_S (°C)	T_L (°C)	$T_{\gamma'}$ (°C)	Freezing range (°C)	Hot processing window (°C)
CNS1	Actual	1285	1351	1150	66	135
	Predicted	1239	1339	1110	112	129
CNS2	Actual	1285	1346	1165	61	120
	Predicted	1239	1339	1116	100	123
CNS3	Actual	1275	1346	1134	71	141
	Predicted	1124	1341	1092	117	132

Fig. 8 shows the SEM micrographs of aged samples, which determined the double phase γ and γ′ structure indicated by blue and red arrows, respectively. From Fig. 8, there was no considerable difference in the γ′ size between the CNS1, CNS2, and CNS3 aged samples. However, the γ′ volume fraction varied between ≈44 % (in the case of CNS3) and ≈68 % (for CNS1 and CNS2). The charactristic γ′ morphology observed in the aged samples (Fig. 8) can be related to the differences in partitioning of elements in γ and γ′ phases. In addition, the γ′ shape deviation in CNS2 and CNS3 samples (Figs. 8b and c) from the cubic morphology in CNS1 (Fig. 8a) indicates a change in γ/γ′ misfit value. The origin of these different microstructural features in samples with different chemical compositions will be discussed in the next sections.

Fig. 9 shows a typical grain boundary micrograph and related chemical analyses from the CNS1 sample after homogenization at 1250 °C followed by air cooling and aging at 900 °C followed by water quenching. The representative back-scattered image and its corresponding mapping analysis revealed a black particle and two types of precipitations at the grain boundary. The black particle is related to the impurity during casting, and it is an Al oxide at the core (indicated by a white arrow) surrounded by a Ti nitride shell (shown by yellow arrows). According to the CALPHAD results for the CNS1 alloy, it is not expected to observe TCPs at the grain boundary. But according to the EDS mapping results, the discontinuous white particles are related to the μ phase (circled in red) enriched with Ti, W, and Ta. Also, the appearance of dark gray strips at grain boundaries (indicated by dashed rectangles), which are enriched with Co and Cr, are the γ′ precipitate-depleted zones (PDZ) and mostly appear in the vicinity of the TCPs [18, 22, 31]. In the case of CNS2 and CNS3 alloys, a small amount of μ phase at the grain boundaries was observed without PDZ strips (supplementary material, Figs. **S1** and **S2**).

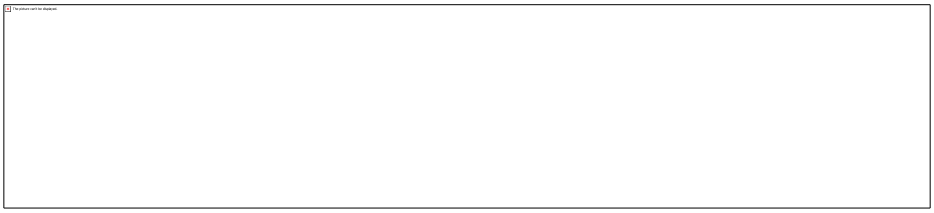

Fig. 8. SEM micrographs of the samples aged at 900 °C for 24h and water quenched: (a) CNS1, (b) CNS2, and (c) CNS3. Red and blue arrows refer to γ and γ′ phases, respectively.

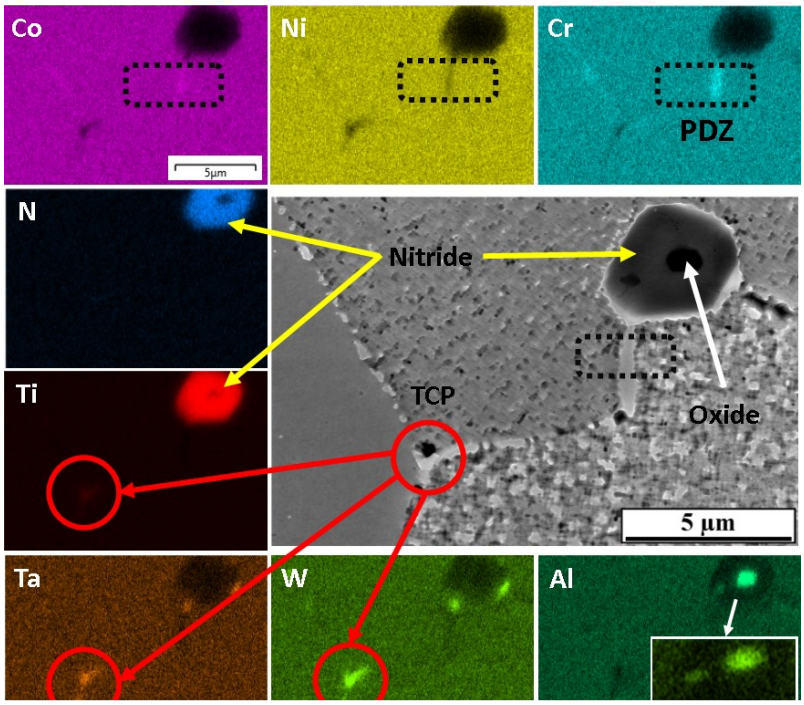

Fig. 9. A typical back-scattered SEM micrograph of grain boundaries and corresponding EDS maps in CNS1 alloy after homogenization at 1250 °C followed by air cooling and aged at 900 °C followed by water quenching.

3.4 Mechanical properties

Nano-indentation maps were employed to confirm the homogenization treatment of as-cast alloys. For example, the nano-hardness and reduced modulus maps of as-cast and homogenized CNS3 alloy are illustrated in Fig. 10. In the vicinity of the B_2 phase in the as-cast alloy (Fig. 10a), the nano-hardness and reduced modulus showed higher and lower values compared to other areas of alloy, respectively. However, after homogenization, the nano-hardness and reduced modulus had a uniform distribution (Fig. 10b), which confirmed the elimination of the B_2 phase. The micro-hardness values of the developed alloys at their different as-cast, homogenized, and aged conditions are plotted in Fig. 11a for comparison, which showed higher hardness values in CNS1 alloy compared to other alloys in all conditions. In addition, homogenization caused a reduction in hardness of the alloys. Moreover, after aging process, the maximum hardness of the alloys was obtained.

The load-depth curve, hardness, and yield strength values calculated from nano-indentation data are illustrated in Fig. 11b. From Fig. 11b, CNS1 alloy had the highest hardness (in agreement with the micro-hardness results) and reduced modulus among the samples, where, the CNS2 alloy revealed the lowest corresponding values. The obtained values for hardness are in good accordance with literature [18, 22]. It should be noted that the difference in hardness values between the γ and γ′ phases could not be directly measured due to the fine size of the γ′ phase. Therefore, all hardness values depict the average hardness across the microstructure for each respective alloy.

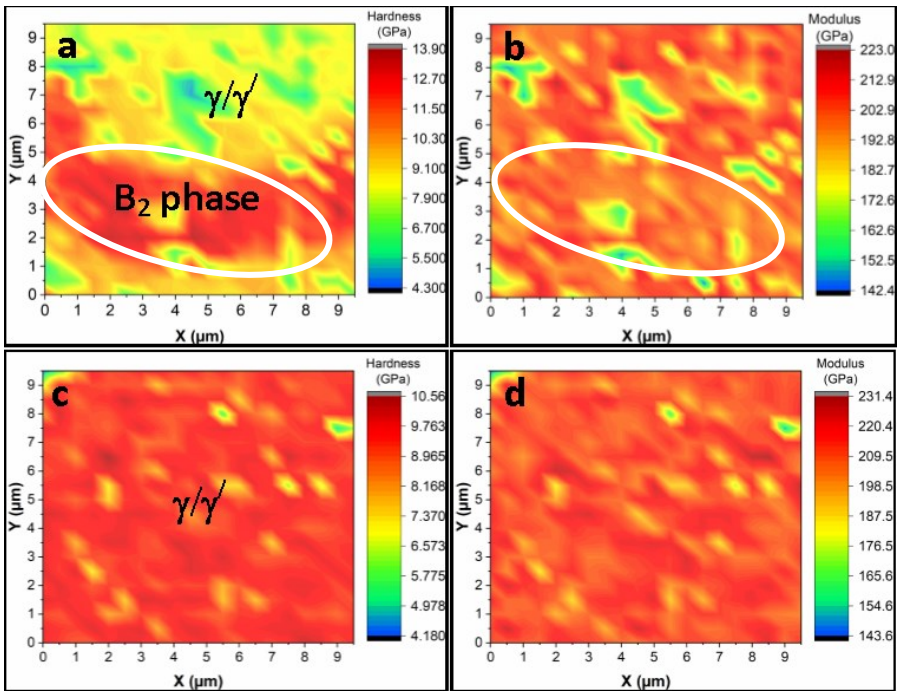

Fig. 10. Nano-hardness and reduced modulus maps of the CNS3 sample obtained from nano-indentation test: (a) as-cast-alloy and (b) homogenized condition. The white ellipse in (a and b) refer to the vicinity of the B_2 phase with lower modulus.

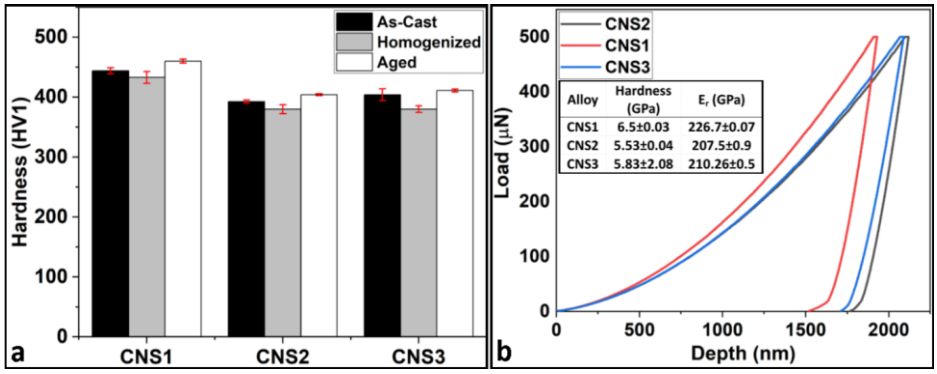

Fig. 11. (a) Micro-hardness distribution of developed alloys in their as-cast, homogenized, and aged conditions. (b) The load-depth plot of the aged samples and their corresponding hardness and reduced modulus were obtained from the nano-indentation test.

4 Discussion

4.1 Effect of ΔS^{mix}

High angle annular dark field (HAADF) STEM image, bright-field TEM images, and corresponding STEM-EDS maps of different elements of alloys CNS1, CNS2, and CNS3 homogenized at 1250 °C for 24h, followed by air cooling and aged at 900 °C for 24h, followed by water quenching, are illustrated in Figs. 12 and 13. In addition, the γ′/γ partitioning coefficient ($K_{\gamma'/\gamma}$) plot for different elements, calculated from STEM-EDS line scan analysis, is illustrated in Fig. 14. The chemical composition, $K_{\gamma'/\gamma}$, and ΔS^{mix} of γ and γ′ phases are summarized in Table 3. From Figs. 12-14, Ti, Ta, Al, Ni, and W (γ′ stabilizers) tend to be partitioned in γ′ phase. Regarding $K^{W}_{\gamma'/\gamma}$ values, i.e. 1.05, 1.02, and 1.04 for CNS1, CNS2, and CNS3 alloys, respectively, W is not a strong γ′ former compared to Ti, Ta, Al, and Ni. Since in developing CoNi based superalloys decreasing the density is essential, W can be replaced with a lighter and affordable γ′ former. According to $K^{Co}_{\gamma'/\gamma}$ and $K^{Cr}_{\gamma'/\gamma}$, Co and Cr (γ stabilizers) are partitioned into γ phase, which are in good agreement with the literature [27, 32]. However, according to the $K^{V}_{\gamma'/\gamma}$ values of 0.95 and 0.92 for CNS2 and CNS3, respectively, and STEM-EDS maps for V in Fig. 13, it has a neutral effect on the amount of γ and γ′ phases, which has not been reported in the literature.

The comparison between the chemical compositions of CNS1 and CNS2 alloys (Table 1) reveals that the amount of Cr is reduced from 13 to 9 at. % and the amount of V is increased from 0 to 4 at. %. Regarding $K_{\gamma'/\gamma}$ variations of CNS1 and CNS2 alloys (Fig. 14), V addition and lowering of

the Cr caused a decrease in $K_{\gamma'/\gamma}^{Ni}$(from 1.61 to 1.48), an increase in $K_{\gamma'/\gamma}^{Al}$ (from 1.57 to 1.77), and an enhancement in $K_{\gamma'/\gamma}^{Co}$ (from 0.77 to 0.82) in CNS2 compared to CNS1. Despite the γ stabilizing effect of Cr and neutral effect of V (Figs. 12-14), the amount of γ′ phase is not changed (≈68 % for CNS1 and CNS2), which indicates the existence of a positive metallurgical parameter compensating the negative effect of Cr on the γ′ volume fraction. In fact, increasing the ΔS^{mix} value from 1.488R to 1.568R by the addition of V at the expense of Cr stabilizes the γ′ phase, and accordingly, it enhances the $T_{\gamma'}$ from 1150 to 1165 °C (Fig. 7 and Table 2).

The developed alloys in the current study are based on well-known CoNi-based superalloy recommended by Lass [8] and Zhuang et al. [18]. ΔS^{mix} and γ′ solvus temperature for the developed alloy in [18] is 1.457R and 1099 °C, respectively. By increasing of its entropy from 1.457R to 1.488R in CNS1 alloy, the γ′ solvus temperature increased from 1099 °C to 1150 °C (approximately 55 °C). In terms of sustainability concept, particularly in the case of superalloys, it is vital to apply more selection and design procedures (pre-build strategies) to increase the high temperature service capability that directly depends on the γ′ solvus temperature. Thus, an enhacement in γ′ solvus tempereature by 55 °C in CNS1 confirms its improved high temperature capability compared to designed alloy by Zhuang et al. [18].

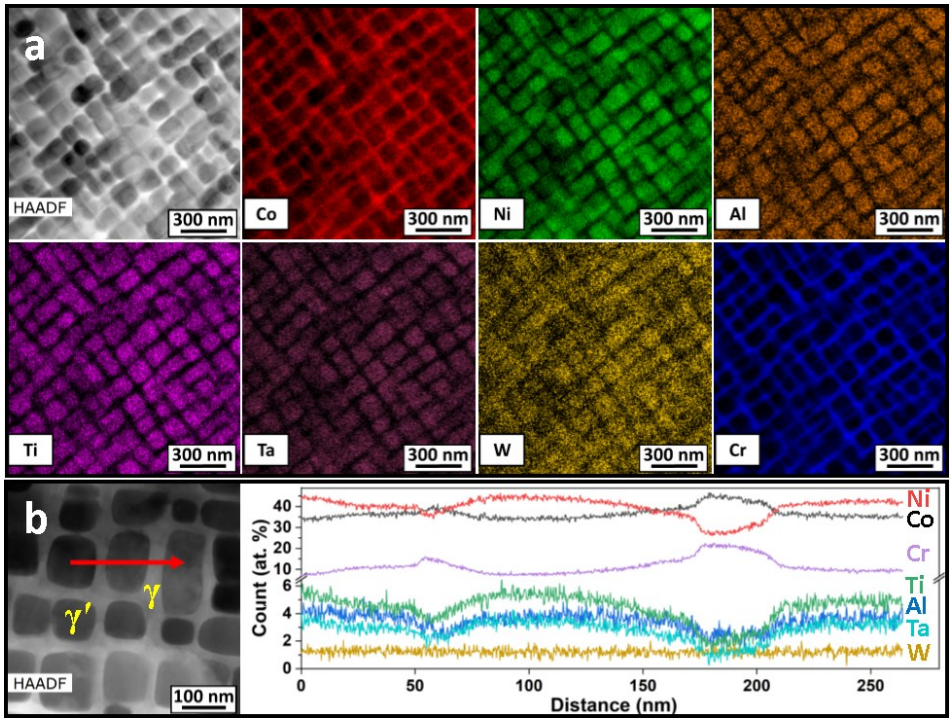

Fig. 12. (a) High angle annular dark field (HAADF) STEM image and corresponding STEM-EDS maps of different elements and (b) a typical STEM-EDS line scan from γ′ and γ phases of alloy CNS1 aged at 900 °C for 24 h followed by water quenching.

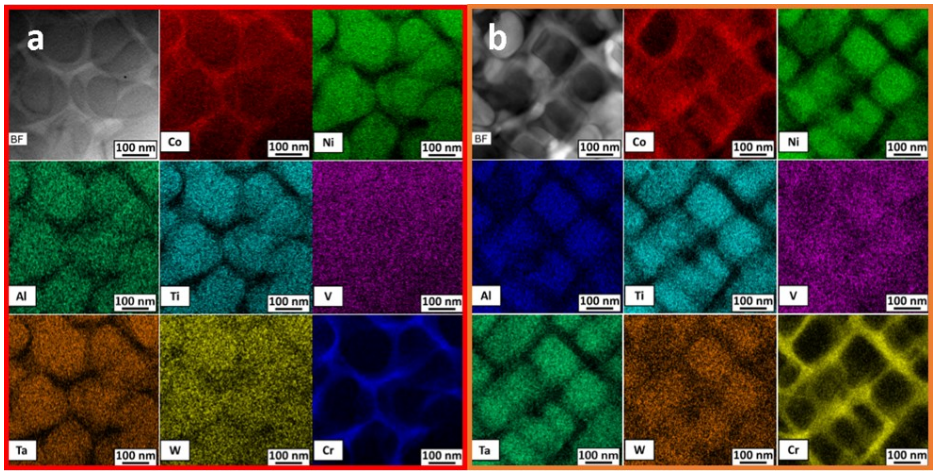

Fig. 13. (a) BF TEM images and corresponding STEM-EDS maps of different elements of alloys CNS2 and CNS3 homogenized at 1250 °C for 24h followed by air cooling and aged at 900 °C for 24 h followed by water quenching.

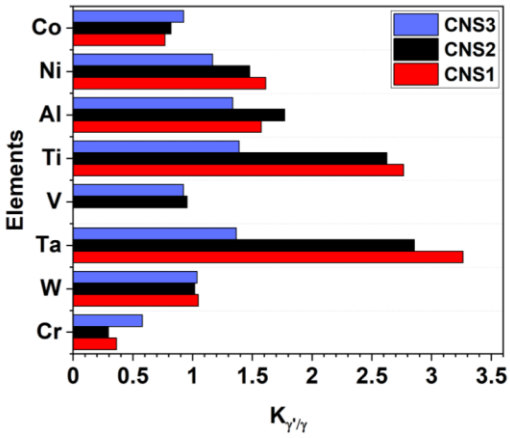

Fig. 14. γ′/γ partitioning coefficients obtained from STEM-EDS analysis of alloys CNS1, CNS2, and CNS3 after homogenization at 1250 °C for 24h followed by air cooling and aging at 900 °C for 24h followed by water quenching.

Table 3. Chemical composition, $K_{\gamma'/\gamma}$, and ΔS^{mix} of the γ and γ′ phases in different alloys. $K_{\gamma/\gamma'}$ was obtained from STEM-EDS line scans by averaging corresponding thirty points.

		Chemical composition (at. %)								
		Co	**Ni**	**Al**	**Ti**	**V**	**Ta**	**W**	**Cr**	**ΔS^{mix}**
γ′	**CNS1**	34.26	44.13	3.73	5.40	0.00	3.48	1.26	7.73	1.378R
	CNS2	35.71	41.79	4.52	4.15	3.70	3.52	1.49	5.13	1.459R
	CNS3	39.15	36.03	5.74	4.97	1.86	3.05	1.55	7.66	1.49R
γ	**CNS1**	44.67	27.37	2.37	1.95	0.00	1.07	1.20	21.36	1.312R
	CNS2	43.58	28.31	2.55	1.58	3.88	1.23	1.46	17.39	1.425R
	CNS3	42.29	30.87	4.30	3.58	2.01	2.23	1.50	13.22	1.475R
$K_{\gamma'/\gamma}$	**CNS1**	0.77	1.61	1.57	2.77	0.00	3.26	1.05	0.36	-
	CNS2	0.82	1.48	1.77	2.62	0.95	2.86	1.02	0.29	-
	CNS3	0.93	1.17	1.33	1.39	0.92	1.36	1.04	0.58	-

4.2 Importance of γ′ stabilizers

To unravel the effect of γ′ stabilizers, the amount of Ni was reduced from 35 to 30 at.%. In addition, the amount of V was reduced from 4 to 2 at. %, while the amount of Co and Cr were increased from 36 to 40 at. % and 9 to 12 at. %, respectively. This chemical composition was selected to keep constant the entropy value in CNS2 and CNS3, i.e. ΔS^{mix}=1.568R (Table 1). The comparison between the microstructural features of CNS2 and CNS3 alloys (Figs. 8 and 13b) discloses that despite the constant value of ΔS^{mix}, the amount of γ′ phase was reduced (from ≈68 % for CNS2 to ≈44 % for CNS3). Moreover, the $T_{\gamma'}$ was reduced from 1165 to 1134 °C (Fig. 7 and Table 2). It can be concluded that ΔS^{mix} and the amount of γ′ stabilizers are competing parameters determining the γ′ phase volume fraction and its corresponding $T_{\gamma'}$. Therefore, during alloy design, based on the high entropy concept, the amount of γ′ stabilizing elements should be considered more conservatively. Also, in the case of Ti and Ta, there is an optimum amount for each element in a way to avoid γ′ precipitates coarsening during aging, a maximum of 4 at. % of Ti is recommended

[10]. Moreover, an optimum value for Ta is lower than 3 at. % to prevent TCPs [8]. Therefore, according to the findings of this research and literature, ***for improving the high temperature performance of CoNi based superalloys, a practical strategy is increasing the ΔS^{mix} using γ' stabilizers***. For comparison, the $T_{\gamma'}$ of developed alloys in this study and other high Cr CoNi-superalloys versus ΔS^{mix} are plotted in Fig. 15. From Fig. 15, the developed alloys possess considerably higher $T_{\gamma'}$ compared to those reported in the literature [14, 18, 31, 33-35]. In addition, it confirms that both the type and the number of elements affect the final $T_{\gamma'}$. It is worth noting that the suggested strategy has some evidence in literature in the case of Ni based superalloys [9]. For instance, the superior high temperature properties of the sixth generation of superalloy TMS238 is due to a ΔS^{mix} of 1.68R, because the TMS alloying system contains 10 elements and the existence of some refractory elements such as Re and Ru.

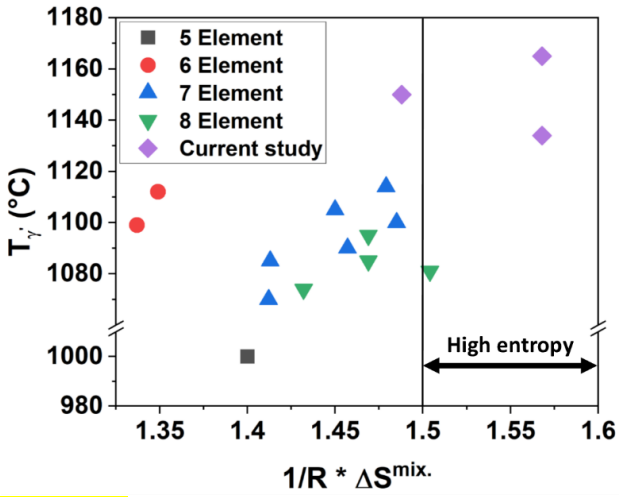

Fig. 15. Effect of the number of elements and ΔS^{mix} on $T_{\gamma'}$ in high Cr CoNi superalloys. Data are collected from the literature [14, 18, 31, 33-35].

4.3 γ' morphology

Elastic stress and interfacial energy between γ and γ′ phases are the most influential experimental parameters that determine the final morphology of the precipitates, i.e. γ′ phase in superalloys. If elastic stress, which is a function of lattice misfit between γ and γ′ phases, acts as the predominant factor, the morphology of the γ′ phase tends to be cubic. On the other hand, when the amount of lattice misfit or elastic stress is low, the interfacial energy will be the governing parameter during coarsening of the γ′ phase [36-38]. In this study, Cr is added to the HEAs to enhance the oxidation resistance. However, it also has a strong tendency to be partitioned into γ (Figs. 12-14), which can reduce the lattice misfit. From Fig. 12, γ′ phase has a cubic morphology despite the existence of high Cr value (13 at. %) in chemical composition of the CNS1 alloy. Therefore, it can be concluded that the alloy design based on high configurational entropy concept (ΔS^{mix}=1.488 in CNS1 alloy) compensates the negative effect of Cr on lattice misfit, and hence the γ′ phase maintains the cubic morphology. It is worth noting that the morphology and volume fraction of γ′ phase determine the final hardness and yield strength of the superalloys [27]. From Fig. 11, the CNS1 alloy possesses the highest values of hardness and yield strength compared to those of the CNS2 and CNS3 thanks to the cubic morphology and high volume fraction of the γ′ phase (≈68 %). On the other hand, CNS1 has lower $T_{\gamma'}$ than CNS2 (Fig. 7 and Table 2).

Despite the lower Cr value in CNS2 compared to CNS1 (lattice misfit ↑) and higher ΔS^{mix} (lattice misfit ↑), the γ′ have changed from cubic to round morphology (Figs. 12 and 13). V tends to have uniform distribution within γ and γ′ phases (Figs. 12-14) ; hence, it can not considerably affect the lattice misfit. Therefore, the possible mechanism is the positive effect of V on interfacial energy, which produces a more rounded γ′ phase. In addition, from Figs. 12 and 13, there are more concentrations of γ′ stabilizing elements (such as Ti, Ta, Al, and Ni) in the interfacial area between γ and γ′ phases, which indicates that V hinders their diffusive ability into the γ′ phase, which can

have a negative effect on the lattice misfit. Totally, because the $K^{V}_{\gamma'/\gamma}$ is approximately equal to 1, it indirectly affects the interfacial energy and lattice misfit by affecting the diffusion of other elements. In CNS3 compared to CNS2 (constant ΔS^{mix}), higher amounts of Co and Cr, which have a high partitioning tendency to γ phase (lattice misfit ↓), and a lower amount of Ni, which has a high partitioning tendency to γ′ phase as it is a strong γ′ stabilizer (lattice misfit ↓), result in the dominance of interfacial energy. Hence, the morphology of γ′ phase tends to be a more rounded shape than the cubic one (Fig. 8).

5 Conclusions

To enhance the high temperature performance of high Cr CoNi-based superalloys, different alloys were designed by CALPHAD simulation and produced based on the high configurational entropy concept for future sustainable manufacturing technologies. The following conclusions can be summarized:

1. Thermomechanical CALPHAD calculation predicts the final microstructures of the designed CoNi-based HESAs with good accuracy. After casting, the microstructures are composed of an FCC matrix (γ phase) containing micro-segregations and B_2 phase. Homogenization treatment at 1250 °C for 24 h followed by air-cooling results in a homogenized and more appropriate microstructure for aging rather than that of followed by furnace-cooling. After aging different volume fractions and morphologies of γ' forms within the γ matrix in the developed alloys.
2. Increasing the ΔS^{mix} can compensate for the negative effect of the γ stabilizers such as Cr, which can be made by even a neutral alloying element such as V. Therefore, by addition of

V at the expense of Cr, ΔS^{mix} stabilizes the γ′ phase. Accordingly, it enhances the γ' solvus temperature.

3. In addition to ΔS^{mix}, the type of alloying elements has a key role in determining the final γ' solvus temperature and volume fraction. During alloy design, to increase the ΔS^{mix}, the amount of γ' stabilizers should not be decreased. Therefore, an excellent strategy to enhance the high temperature characteristics is increasing the ΔS^{mix} by increasing the amount of γ′ stabilizers in chemical composition.
4. Using the presented strategy, CoNi based HESAs with high γ' solvus temperatures (1165 °C), large processing window (120 °C-141 °C), large freezing range (61 °C-71 °C), and hardness values comparable with the recently developed CoNi based superalloys can be produced. These characteristics make the developed alloys promising materials for sustainable manufacturing technologies such as powder bed fusion technologies, which can be a hot topic for future research.

CRediT authorship contribution statement

Ahad Mohammadzadeh: Conceptualization, Methodology, Data and experiments curation and analysis, Funding and Investigation, Writing-original draft, Writing-review & editing. **Akbar Heidarzadeh**: Conceptualization, Methodology, Investigation, Writing-review & editing. **Hailey Becker**: TEM and nanoindentation study as a part of her internship project, Writing-review & editing. **Jorge Valilla Robles**: CALPHAD study, Writing-review & editing. **Alberto Meza**: Investigation, sample preparation, casting, review & editing. **Manuel Avella**: TEM test, review & editing. **Miguel Monclús**: nanoindentation test, review & editing. **Damien Tourret**: CALPHAD

study, writing-review & editing. **Jose M. Torralba**: Conceptualization, Resources, Project administration, Writing-review & editing, Supervision.

Declaration of competing interest

The authors declare no conflict of interest.

Data availability statement

The raw/processed data required to reproduce these findings cannot be shared at this time as the data also forms part of an ongoing study.

Acknowledgment

This investigation was supported by the European Union Horizon 2020 research and innovation programme (Marie Sklodowska-Curie Individual Fellowships, Grant Agreement 101028155). A portion of the funding for this research was supported by National Science Foundation Division of Material Research (Grant No. DMR2153316) through the International Research Experience for Students (IRES) program. Amalia Sanromán and Ignacio Escobar are sincerely thanked for their help with VAR processing and sample preparations.

References

[1] H. Al Baroudi, A. Awoyomi, K. Patchigolla, K. Jonnalagadda, E.J. Anthony, A review of large-scale CO2 shipping and marine emissions management for carbon capture, utilisation and storage, Applied Energy 287 (2021) 116510.
[2] L. Ren, S. Zhou, T. Peng, X. Ou, A review of CO2 emissions reduction technologies and low-carbon development in the iron and steel industry focusing on China, Renewable and Sustainable Energy Reviews 143 (2021) 110846.
[3] B. Cao, Y. Zhao, T. Yang, C.T. Liu, L12-Strengthened Co-Rich Alloys for High-Temperature Structural Applications: A Critical Review, Advanced Engineering Materials 23(10) (2021) 2100453.

[4] D. Migas, G. Moskal, H. Myalska, T. Mikuszewski, The effect of alloying elements on oxide scale spallation of multicomponent Co-based superalloys, Corrosion Science 192 (2021) 109787.
[5] E.A. Lass, D.J. Sauza, D.C. Dunand, D.N. Seidman, Multicomponent γ′-strengthened Co-based superalloys with increased solvus temperatures and reduced mass densities, Acta Materialia 147 (2018) 284-295.
[6] J. Sato, T. Omori, K. Oikawa, I. Ohnuma, R. Kainuma, K. Ishida, Cobalt-base high-temperature alloys, Science 312(5770) (2006) 90-91.
[7] W. Li, L. Li, S. Antonov, Q. Feng, Effective design of a Co-Ni-Al-W-Ta-Ti alloy with high γ′ solvus temperature and microstructural stability using combined CALPHAD and experimental approaches, Materials & Design 180 (2019) 107912.
[8] E.A. Lass, Application of computational thermodynamics to the design of a Co-Ni-based γ′-strengthened superalloy, Metallurgical and Materials Transactions A 48(5) (2017) 2443-2459.
[9] J.-W. Yeh, S.-J. Lin, Breakthrough applications of high-entropy materials, Journal of Materials Research 33(19) (2018) 3129-3137.
[10] P. Pandey, S. Mukhopadhyay, C. Srivastava, S.K. Makineni, K. Chattopadhyay, Development of new γ′-strengthened Co-based superalloys with low mass density, high solvus temperature and high temperature strength, Materials Science and Engineering: A 790 (2020) 139578.
[11] F.L. Reyes Tirado, S. Taylor, D.C. Dunand, Effect of Al, Ti and Cr additions on the γ-γ′ microstructure of W-free Co-Ta-V-Based superalloys, Acta Materialia 172 (2019) 44-54.
[12] S.K. Makineni, B. Nithin, K. Chattopadhyay, A new tungsten-free γ–γ′ Co–Al–Mo–Nb-based superalloy, Scripta Materialia 98 (2015) 36-39.
[13] M. Knop, P. Mulvey, F. Ismail, A. Radecka, K. Rahman, T. Lindley, B. Shollock, M. Hardy, M. Moody, T. Martin, A new polycrystalline Co-Ni superalloy, Jom 66(12) (2014) 2495-2501.
[14] Y. Guan, Y. Liu, Z. Ma, H. Li, H. Yu, Investigation on γ′ stability in CoNi-based superalloys during long-term aging at 900 °C, Journal of Alloys and Compounds 842 (2020) 155891.
[15] P. Liu, H. Huang, S. Antonov, C. Wen, D. Xue, H. Chen, L. Li, Q. Feng, T. Omori, Y. Su, Machine learning assisted design of γ′-strengthened Co-base superalloys with multi-performance optimization, npj Computational Materials 6(1) (2020) 62.
[16] M. Wen, Y. Sun, J. Yu, Y. Yang, Y. Zhou, X. Sun, Effects of Al content on microstructures and high-temperature tensile properties of two newly designed CoNi-base superalloys, Journal of Alloys and Compounds 835 (2020) 155337.
[17] C.A. Stewart, S.P. Murray, A. Suzuki, T.M. Pollock, C.G. Levi, Accelerated discovery of oxidation resistant CoNi-base γ/γ′alloys with high L12 solvus and low density, Materials & Design 189 (2020) 108445.
[18] X. Zhuang, S. Lu, L. Li, Q. Feng, Microstructures and properties of a novel γ′-strengthened multi-component CoNi-based wrought superalloy designed by CALPHAD method, Materials Science and Engineering: A 780 (2020) 139219.
[19] J. Ruan, X. Liu, S. Yang, W. Xu, T. Omori, T. Yang, B. Deng, H. Jiang, C. Wang, R. Kainuma, Novel Co-Ti-V-base superalloys reinforced by L12-ordered γ′ phase, Intermetallics 92 (2018) 126-132.
[20] B.X. Cao, H.J. Kong, Z.Y. Ding, S.W. Wu, J.H. Luan, Z.B. Jiao, J. Lu, C.T. Liu, T. Yang, A novel L12-strengthened multicomponent Co-rich high-entropy alloy with both high γ′-solvus temperature and superior high-temperature strength, Scripta Materialia 199 (2021) 113826.

[21] G. Xiao, J. Jiang, Y. Wang, Y. Liu, Y. Zhang, Microstructure and mechanical properties of nickel-based superalloy GH4037 parts formed by thixoforming, Materials Science and Engineering: A 780 (2020) 139196.
[22] P.J. Bocchini, C.K. Sudbrack, R.D. Noebe, D.C. Dunand, D.N. Seidman, Effects of titanium substitutions for aluminum and tungsten in Co-10Ni-9Al-9W (at%) superalloys, Materials Science and Engineering: A 705 (2017) 122-132.
[23] W. Li, L. Li, S. Antonov, C. Wei, J.-C. Zhao, Q. Feng, High-throughput exploration of alloying effects on the microstructural stability and properties of multi-component CoNi-base superalloys, Journal of Alloys and Compounds 881 (2021) 160618.
[24] W. Li, L. Li, C. Wei, J.-C. Zhao, Q. Feng, Effects of Ni, Cr and W on the microstructural stability of multicomponent CoNi-base superalloys studied using CALPHAD and diffusion-multiple approaches, Journal of Materials Science & Technology 80 (2021) 139-149.
[25] F.L. Reyes Tirado, J. Perrin Toinin, D.C. Dunand, γ+γ′ microstructures in the Co-Ta-V and Co-Nb-V ternary systems, Acta Materialia 151 (2018) 137-148.
[26] Y. Chen, C. Wang, J. Ruan, T. Omori, R. Kainuma, K. Ishida, X. Liu, High-strength Co–Al–V-base superalloys strengthened by γ′-Co3(Al,V) with high solvus temperature, Acta Materialia 170 (2019) 62-74.
[27] Z. Liang, S. Neumeier, Z. Rao, M. Göken, F. Pyczak, CALPHAD informed design of multicomponent CoNiCr-based superalloys exhibiting large lattice misfit and high yield stress, Materials Science and Engineering: A 854 (2022) 143798.
[28] A. Bauer, S. Neumeier, F. Pyczak, M. Göken, Microstructure and creep strength of different γ/γ′-strengthened Co-base superalloy variants, Scripta Materialia 63(12) (2010) 1197-1200.
[29] W.C. Oliver, G.M. Pharr, An improved technique for determining hardness and elastic modulus using load and displacement sensing indentation experiments, Journal of Materials Research 7(6) (1992) 1564-1583.
[30] X. Zhuang, S. Antonov, W. Li, S. Lu, L. Li, Q. Feng, Alloying effects and effective alloy design of high-Cr CoNi-based superalloys via a high-throughput experiments and machine learning framework, Acta Materialia 243 (2023) 118525.
[31] Y. Zhang, H. Fu, X. Zhou, Y. Zhang, J. Xie, Effects of aluminum and molybdenum content on the microstructure and properties of multi-component γ′-strengthened cobalt-base superalloys, Materials Science and Engineering: A 737 (2018) 265-273.
[32] Y. Xu, X. Lv, T. Ma, H. Li, T. Wang, Effect of Ta and Ni on γ′ phase morphology and compression behavior of Co-8.8Al-9.8W superalloys, Materials Science and Engineering: A 839 (2022) 142739.
[33] X. Zhuang, S. Antonov, L. Li, Q. Feng, Effect of alloying elements on the coarsening rate of γ′ precipitates in multi-component CoNi-based superalloys with high Cr content, Scripta Materialia 202 (2021) 114004.
[34] S. Neumeier, L.P. Freund, M. Göken, Novel wrought γ/γ′ cobalt base superalloys with high strength and improved oxidation resistance, Scripta Materialia 109 (2015) 104-107.
[35] M. Knop, P. Mulvey, F. Ismail, A. Radecka, K.M. Rahman, T.C. Lindley, B.A. Shollock, M.C. Hardy, M.P. Moody, T.L. Martin, P.A.J. Bagot, D. Dye, A New Polycrystalline Co-Ni Superalloy, JOM 66(12) (2014) 2495-2501.
[36] C. Che, S. Yang, M. Wei, L. Zhang, Q. Li, J. Gao, Y. Du, Microstructure, hardness and interfacial energy in Co-9Al-10W-xNi (x= 15, 25, 35 at.%) alloys during aging, Journal of Mining and Metallurgy, Section B: Metallurgy 53(3) (2017) 303-303.

[37] W. Wu, U.R. Kattner, C.E. Campbell, J.E. Guyer, P.W. Voorhees, J.A. Warren, O.G. Heinonen, Co-Based superalloy morphology evolution: A phase field study based on experimental thermodynamic and kinetic data, Acta Materialia 233 (2022) 117978.
[38] V.A. Vorontsov, J.S. Barnard, K.M. Rahman, H.Y. Yan, P.A. Midgley, D. Dye, Coarsening behaviour and interfacial structure of γ′ precipitates in Co-Al-W based superalloys, Acta Materialia 120 (2016) 14-23.